



A Unified Framework for Synthesizing Multisequence Brain MRI via Hybrid Fusion

Jihoon Cho^a, Jonghye Woo^b, Jinah Park^{a,*}

^aSchool of Computing, Korea Advanced Institute of Science and Technology, Daejeon 34141, Republic of Korea

^bGordon Center for Medical Imaging, Massachusetts General Hospital and Harvard Medical School, Boston, MA 02114, USA

ARTICLE INFO

Article history:

Received 1 June 2024

Received in final form -

Accepted -

Available online -

Communicated by -

2000 MSC: 41A05, 41A10, 65D05, 65D17

Keywords: Medical Image Synthesis, Hybrid Fusion, Data Imputation, Multisequence MRI

ABSTRACT

Multisequence Magnetic Resonance Imaging (MRI) provides a reliable diagnosis in clinical applications through complementary information within sequences. However, in practice, the absence of certain MR sequences is a common problem that can lead to inconsistent analysis results. In this work, we propose a novel unified framework for synthesizing multisequence MR images, called Hybrid Fusion GAN (HF-GAN). We introduce a hybrid fusion encoder designed to ensure the disentangled extraction of complementary and modality-specific information, along with a channel attention-based feature fusion module that integrates the features into a common latent space handling the complexity from combinations of accessible MR sequences. Common feature representations are transformed into a target latent space via the modality infuser to synthesize missing MR sequences. We have performed experiments on multisequence brain MRI datasets from healthy individuals and patients diagnosed with brain tumors. Experimental results show that our method outperforms state-of-the-art methods in both quantitative and qualitative comparisons. In addition, a detailed analysis of our framework demonstrates the superiority of our designed modules and their effectiveness for use in data imputation tasks.

© 2024 Elsevier B. V. All rights reserved.

1. Introduction

Magnetic Resonance Imaging (MRI) is highly effective in extracting crucial information from soft tissue regions, making it a widely used imaging modality in clinical diagnosis and treatment. By leveraging the intrinsic MR properties of tissues—such as proton density, T1, and T2—and the properties of externally applied excitation, we can acquire various MRI sequences, where each sequence exhibits distinct characteristics, particularly yielding unique contrasts between soft tissues. Considering that the significance of the features varies with the MR sequence, the use of a combination of sequences yields superior results compared to processing a single sequence (Menze

et al., 2014; Schouten et al., 2016). However, acquiring a complete set of multisequence MRI scans can be challenging due to practical issues such as extended scan duration, patient-induced motion artifacts, and varying imaging protocols. Incomplete MR sequences, which lack essential information, lead to inconsistent analysis results, particularly for computer-aided diagnosis methods using deep learning that are sensitive to data distribution (Chan et al., 2020). However, re-scanning the missing MR sequences is not feasible due to the high cost associated with data acquisition.

A common approach to address data imputation in medical imaging is to synthesize missing MR sequences based on available MR sequences. As deep learning-based approaches have advanced in medical imaging, MRI synthesis methods have also been translated into learning-based synthesis methods, such as convolutional neural networks (CNNs) and transformers (Chartsias et al., 2017; Dar et al., 2019; Sevetlidis et al.,

*Corresponding author at: School of Computing, Korea Advanced Institute of Science and Technology, Daejeon, Republic of Korea.
E-mail address: jinahpark@kaist.ac.kr (J. Park).

2016; Yurt et al., 2021; Zhou et al., 2020) from traditional approaches (Lee et al., 2017; Jog et al., 2017; Ye et al., 2013). To take advantage of CNNs, initial research focused on training the relationships between MR sequences by embedding them into a shared latent space (Chartsias et al., 2017), exploring multi-level interactions among sequences (Zhou et al., 2020), and constructing additional architectures to extract complementary information (Yurt et al., 2021). However, these methods are designed for fixed source-target pairs, making them impractical for data imputation tasks in real-world scenarios.

Recent research has increasingly focused on a unified approach that can be used for data imputation tasks (Cho et al., 2024; Dalmaz et al., 2022; Sharma and Hamarneh, 2019; Liu et al., 2021, 2023; Yang et al., 2021), but it still faces challenges related to information loss. For example, they may not fully utilize all available MR sequences due to taking only a single source image (Cho et al., 2024; Liu et al., 2021; Yang et al., 2021), or even if they do, the employed structure might result in suboptimal performance. Fully convolutional networks (FCN) have fundamental limitations in learning long-range dependencies, which can be obstacles to their understanding of the overall structure (Sharma and Hamarneh, 2019). Even with the application of transformer architecture that can capture long-range dependencies, the use of a single multichannel encoder (Dalmaz et al., 2022) or modality-specific encoders (Liu et al., 2023) alone is inadequate for capturing complementary information between MR sequences. Furthermore, they do not guarantee that the latent space is appropriate to handle the complexity of missing MR scenarios, which are $2^N - 2$ cases when N MR sequences are provided.

To address these problems, in this work, we propose a novel unified framework for synthesizing missing MR sequences, called Hybrid Fusion GAN (HF-GAN). HF-GAN can handle all missing scenarios with a single network, fully exploiting the information available from MR sequences. To synthesize the missing sequence, HF-GAN utilizes a hybrid fusion encoder (Cho and Park, 2023) to extract complementary and modality-specific information separately. The extracted features are then projected into a common latent space to facilitate the sharing of essential MR sequence components through a channel attention-based feature fusion module. Subsequently, the feature representations in the common latent space are transformed into the target latent space using the modality infuser (Cho et al., 2024) that employs consecutive self-attention mechanisms, and finally, the target MR sequence is synthesized using the CNN decoder. We conducted experiments using multisequence MRI datasets of healthy brains and brains with tumors. The experimental results show the superiority of the proposed approach both quantitatively and qualitatively. Furthermore, extensive analysis demonstrates that our approach can disentangle the latent space and extract complementary information within sequences. We also performed an ablation study to confirm the effectiveness of our designed modules.

An earlier version of this work has appeared in Cho et al. (2024). Built upon that work, this paper introduces the following improvements. (1) We improve the one-to-one translation method to a many-to-one synthesis method, utilizing all acces-

sible MR images while maintaining a unified approach. (2) We introduce a hybrid fusion encoder designed to ensure the extraction of complementary information, along with a channel attention-based feature fusion module that integrates the feature representations into a common latent space containing crucial information. (3) We carry out comprehensive experiments using the BraTS dataset for patients and the IXI dataset for healthy subjects and demonstrated the effectiveness of our approach through a detailed analysis of our designed modules.

2. Related Work

The synthesis of missing MR sequences from acquired images has recently attracted interest to date. The data-driven approach using deep learning has emerged as a promising solution to address the problem of missing data, particularly with the success of generative adversarial networks (GANs) (Goodfellow et al., 2014). We provide a brief overview of the image synthesis methods, classifying them into three categories: (1) one-to-one synthesis methods, (2) many-to-one synthesis methods, and (3) many-to-many unified synthesis methods.

One-to-One Synthesis Methods synthesize the target modality from a different modality. Dar et al. (2019) introduced pGAN and cGAN for MR image synthesis by translating between T1-weighted and T2-weighted MRI using adversarial training. Xin et al. (2020) proposed TC-MGAN, which generates T1-weighted, post-contrast T1-weighted, and T2-FLAIR images from T2-weighted images. This method can synthesize three modalities with a single network, although the input modality remains fixed. UCD-GAN (Liu et al., 2021) and Hyper-GAN (Yang et al., 2021) demonstrated the possibility of a unified one-to-one synthesis approach capable of managing all modality pairs with a single network by introducing a common latent space. In our previous work, TransMI (Cho et al., 2024), we introduced an effective target modality conditioning mechanism within a unified disentanglement framework. However, a main limitation is its dependence on a single input, even though other modalities are accessible. To overcome this problem, we improve our previous approach to handle all missing scenarios through effective feature extraction and feature fusion.

Many-to-One Synthesis Methods integrate the information from the multiple modalities to synthesize the target modality. Chartsias et al. (2017) demonstrated the shared latent space fusion approach for synthesizing the target modality from individual latent representations. HI-NET (Zhou et al., 2020) demonstrated the effectiveness of feature fusion through the interaction of multi-level representations. DiamondGAN (Li et al., 2019) and CollaGAN (Lee et al., 2020) introduced feature fusion methods from individually extracted features to handle specific missing cases using a unified network. MustGAN (Yurt et al., 2021) showed a novel feature fusion method of the mixture of multiple one-to-one streams for modality-specific information and a joint many-to-one stream for complementary information. However, all of these methods require an additional network to handle all the missing scenarios.

Many-to-Many Unified Synthesis Methods focus on handling all missing MR scenarios using a single network. Sharma

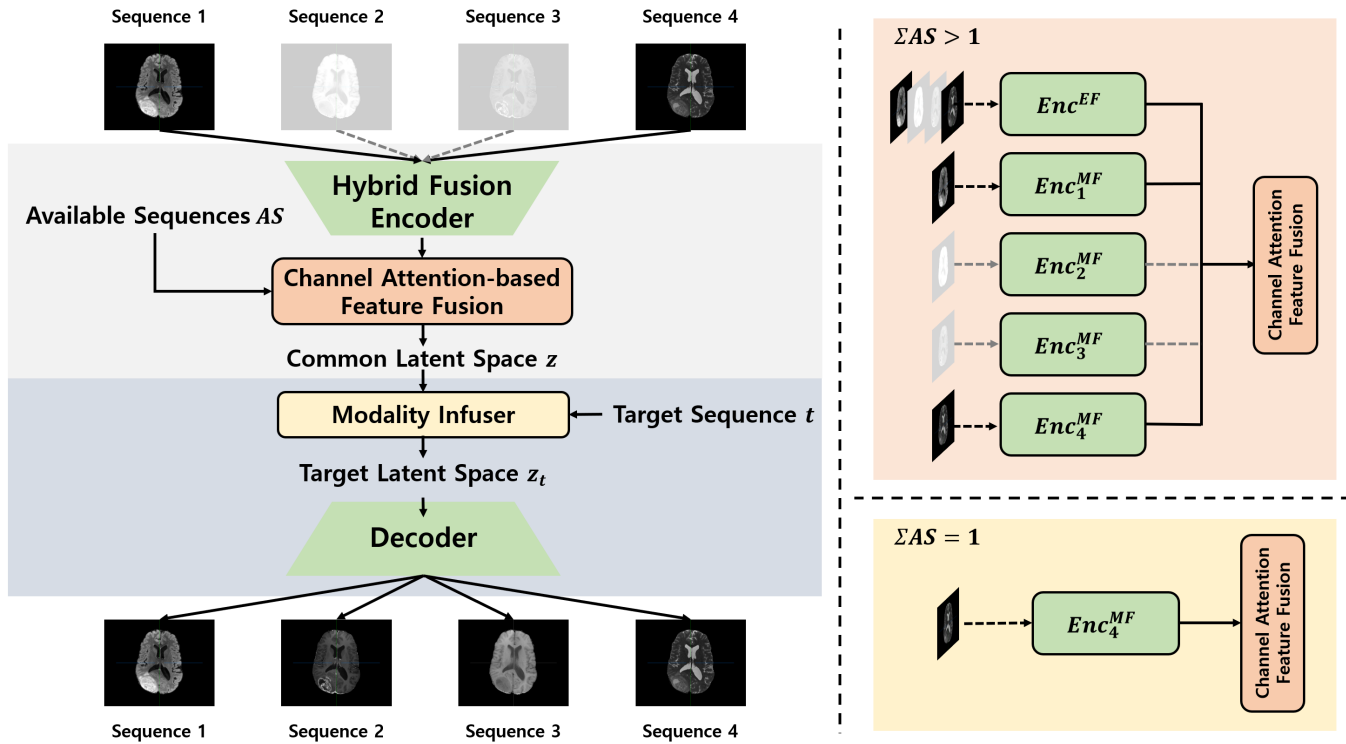


Fig. 1. Illustration of our framework for synthesizing missing MR sequences. (left) Only accessible MR sequences are used to project into a common latent space. The projected feature representations are converted into the target latent space using the modality infuser, and a decoder generates target MR sequences based on the latent space of the feature representation. (right) If there are multiple accessible MR sequences, the complementary features extracted from the early fusion encoder are used.

and Hamarneh (2019) introduced MMGAN, which handles all available modalities and generates the missing ones within a unified encoder-decoder framework. ResViT (Dalmaz *et al.*, 2022) introduced a structure that employs transformer-based bottleneck layers to understand the global context. MM-Trans (Liu *et al.*, 2023) proposed an architecture based entirely on transformers, which requires high computational cost, highlighting its advantage in capturing long-range dependencies. However, these unified approaches still struggle with the complexity of all missing scenarios and the lack of complementary information.

In this work, we propose a novel multisequence MRI synthesis method that is based on the unified one-to-one synthesis method, which has a common latent space to handle various MR sequences. We focus on the extraction of complementary information, which is the key element for the accurate synthesis of MR images, using a hybrid fusion encoder, a channel attention-based fusion module, and the modality infuser consisting of transformer layers.

3. Method

Our unified framework comprises the image generator G to synthesize missing MR sequences and the discriminator D to perform adversarial learning. To achieve the synthesis of all the modality compositions using a single network, our image generator consists of three key modules, including (1) hybrid fusion

encoder Enc^{HF} , which extracts complementary information and modality-specific information through the hybrid fusion approach (Cho and Park, 2023), (2) channel attention-based feature fusion module $CAFF$, which projects the extracted features into a common latent space, and (3) transformer-based modality infuser MI , which facilitates the synthesis of the target modality as in our previous work (Cho *et al.*, 2024). An overview of our framework is shown in Figure 1.

3.1. Hybrid Fusion Encoder

The first process to synthesize missing MR sequences is to extract valuable features from available MR images. The effectiveness of this process largely depends on the encoder’s architecture, and we propose to use the structure of a hybrid fusion encoder for efficient feature extraction by separating different feature representations according to their distinct purpose. Given a set of N MR sequences $I = \{I_i\}_{i=1}^N$, the hybrid fusion encoder Enc^{HF} consists of an early fusion CNN encoder Enc^{EF} to extract complementary information between all N sequences and N of 1-channel middle fusion CNN encoders Enc_i^{MF} ($i = 1, \dots, N$) to extract modality-specific information from each MR sequence. Each encoder shares an identical architecture with five residual blocks consisting of group normalization (Wu and He, 2018), SiLU activation function (Elfwing *et al.*, 2018), and a 2D convolution layer, the only difference being the number of input channels. Our framework serves as a unified synthesis model, so we can handle all missing scenarios

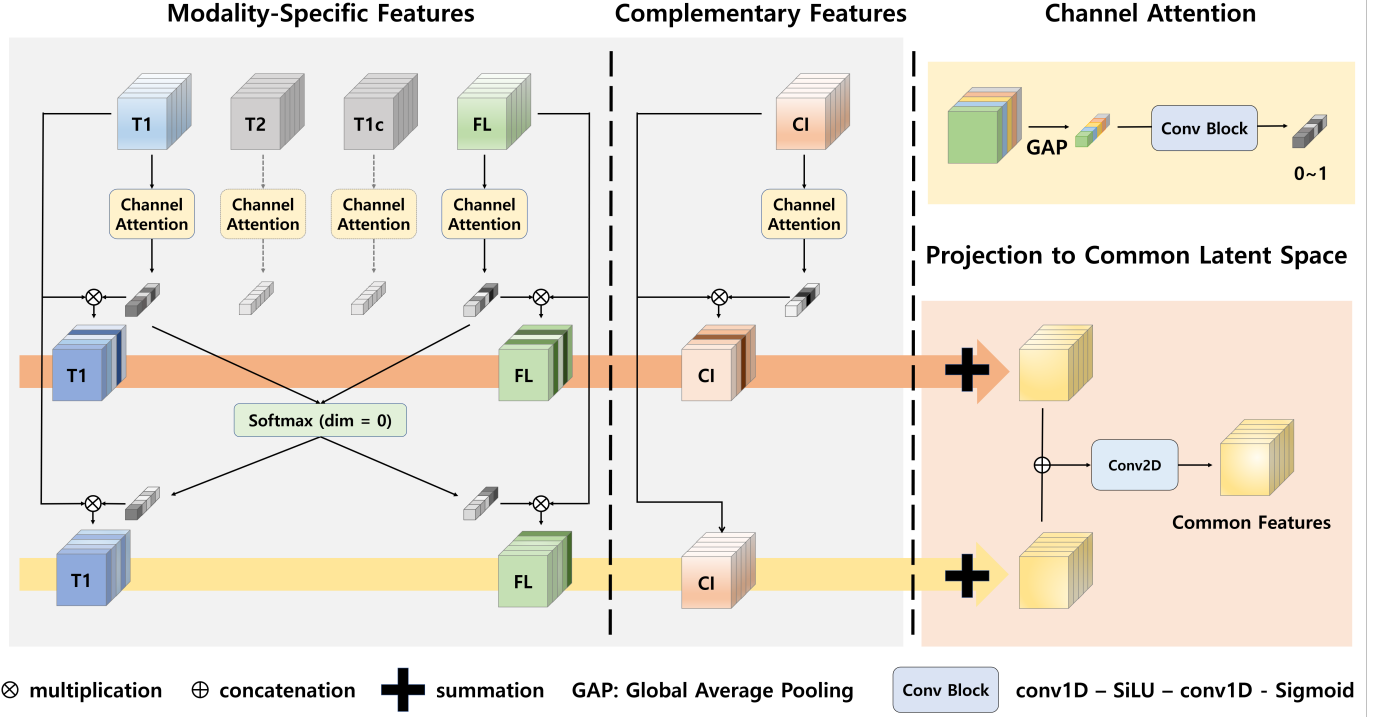


Fig. 2. An example of the channel attention-based feature fusion module *CAFF* for four MR sequences, which are T1, T2, T1c, and FL. *CAFF* has two main fusion paths. (orange arrow) The first path involves the integration of significant features to emphasize essential channels, with importance maps for each feature being computed by channel attention modules. (yellow arrow) The second path functions as a residual path, applying weights to the available MR sequences using recomputed importance maps derived from the softmax operation.

by collecting feature representations F based on the available MR sequences $AS = \{AS_i \in \{0, 1\}\}_{i=1}^N$, formulated as

$$\begin{aligned} F &= Enc^{HF}(X) \\ &= \{Enc^{EF}(X), Enc_i^{MF}(X_i) (i = 1, \dots, N)\}, \end{aligned} \quad (1)$$

where $X = \{X_i\}_{i=1}^N = \{I_i \cdot AS_i\}_{i=1}^N$ are input images with masking of missing MR sequences.

3.2. Channel Attention-based Feature Fusion

A collection of feature representations F has been extracted from the hybrid fusion encoder. The total $2^N - 2$ cases of the available MR sequences pose a challenge in how to integrate all feature representations while preserving important features. However, a straightforward method such as the max function (Chartsias et al., 2017) cannot guarantee the handling of all missing scenarios, and, in particular, complementary information requires unique processing as it is distinct from modality-specific information. To address this issue, we propose the channel attention-based feature fusion module *CAFF* that can dynamically integrate feature representations while preserving important information. The proposed *CAFF* can capitalize on crucial features and prevent loss of channel information while highlighting significant MR sequences and preserving complementary information. As in Figure 2, only feature representations from available images are used and feature representation that contains complementary information is also used

when multiple modalities are present. Importance maps for each channel are computed using channel attention to highlight significant features and eliminate irrelevant ones. These importance maps additionally adjust the significance across the available MR sequences through the softmax operation, which is applied only to modality-specific features. Finally, a set of feature representations F is transformed into a common latent space z by *CAFF* to allow projection into a consistent space regardless of the composition of available MR sequences:

$$z = CAFF(F, AS). \quad (2)$$

3.3. Modality Infuser

To synthesize the target of missing MR sequence $t \in \{1, \dots, N\}$, auxiliary information about the target MR sequence is necessary. Target indicators are typically added as extra channels within the latent space (Liu et al., 2021; Mirza and Osindero, 2014). However, the capability to synthesize the target modality depends on the decoder structure, and the additional operations to decode these indicators may degrade the performance of the synthesis. Therefore, we propose a powerful conditioning approach through feature-level conversion, which transforms feature representations from a common latent space to the specific latent space of the target sequence. We employ the architecture of the modality infuser *MI* (Cho et al., 2024). The architecture includes $L (= 4)$ transformer layers, which are placed after the positional encoding and the modality encoding as in Figure 3. The common feature representations z are

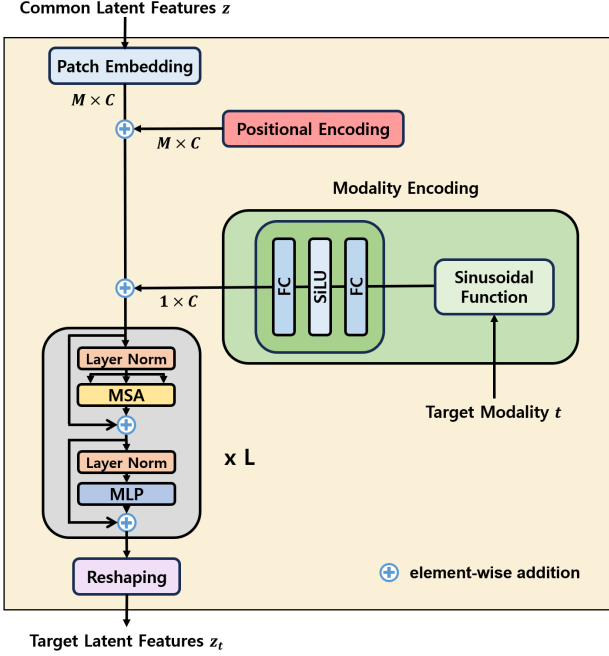


Fig. 3. The structure of the modality infuser MI . The target modality is encoded by learning parameters based on sinusoidal function and added to all 1D tokens.

transformed into M 1D tokens $s_0 \in \mathbb{R}^{M \times C}$ by the patch embedding process. Positional encoding adds unique spatial representations to these sequences, facilitating comprehension of the overall structure (Dosovitskiy et al., 2020). Subsequently, the 1D tokens s_0 undergo L successive rounds of processing by the self-attention layers, with modality encoding $ME \in \mathbb{R}^{1 \times C}$ based on the sinusoidal function \sinus defined as

$$\begin{aligned} \sinus(t, 2i) &= \sin\left(\frac{t}{10000^{\frac{2i}{C}}}\right), \\ \sinus(t, 2i+1) &= \cos\left(\frac{t}{10000^{\frac{2i+1}{C}}}\right), \end{aligned} \quad (3)$$

where C is the channel dimension of the 1D tokens, $2i$ and $2i+1$ are the channel indices.

The \sinus serves as the target MR sequence indicator for modality encoding, and learnable parameters are employed as

$$ME = MLP(\sinus(t)), \quad (4)$$

where MLP denotes the multi-layer perceptron, which is composed of fully-connected layers and a non-linear activation function.

The 1D tokens s_L are reshaped back to the original dimensions of the latent feature representations to form the feature representation of the target modality z_t . These latent feature representations are fed into the CNN decoder Dec , which has a similar architecture to the CNN encoder but uses skip-connection and up-sampling instead of strided convolution, to synthesize the target images \tilde{y}_t without an additional target indicator, can be written as

$$\tilde{y}_t = G(X, AS, t) = Dec(MI(z, t)) = Dec(z_t). \quad (5)$$

3.4. Training loss

We have assumed spatially co-registered MR sequences so that the synthesized images can be directly compared with the actual image x_t using the L1 loss defined as

$$L_{rec} = |x_t - \tilde{y}_t|. \quad (6)$$

The reconstruction loss ensures that the feature representation comprehensively captures the characteristics of the training data across various MR sequences. The synthesized images \tilde{y}_t are used again to enhance the preservation of shape structures through the cycle-consistency loss L_{cyc} (Zhu et al., 2017) defined as

$$L_{cyc} = |x_c - G(\hat{X}_t, \hat{A}\hat{S}, c)|, \quad (7)$$

where c represents one of the available MR sequences used to synthesize \tilde{y}_t , and \hat{X} and $\hat{A}\hat{S}$ refer to the newly composed MR images and sequences including the synthesized target sequence and excluding the new target sequence c .

Furthermore, the feature similarity loss L_{sim} is applied to establish a common latent space by promoting alignment within the latent space for different input composition of the same subject, and it is defined as

$$L_{sim} = \frac{z \cdot \hat{z}}{\|z\| \cdot \|\hat{z}\|}, \quad (8)$$

where \hat{z} denotes the latent feature representations extracted from the images of the same subject as z , but with a different input composition $\hat{A}\hat{S}$.

For the adversarial training process, we use the discriminator D of PatchGAN (Isola et al., 2017). This discriminator is tasked with discriminating between real and synthetic images and also classifies their modalities. The adversarial loss and the classification loss are defined as follows:

$$L_{adv} = \mathbb{E}_x[\log D(x)] + \mathbb{E}_{\tilde{y}}[1 - \log D(\tilde{y})], \quad (9)$$

$$L_{cls} = \mathbb{E}_{x,c}[-\log D_{cls}(c|x)] + \mathbb{E}_{\tilde{y},t}[-\log D_{cls}(t|\tilde{y})]. \quad (10)$$

Incorporating an auxiliary modality classification task allows training with a single discriminator and helps to construct probability distributions between different modalities (Odena et al., 2017).

The total losses of the image generator and discriminator are defined as the weighted sum of the loss components:

$$L_G = \alpha L_{rec} + \beta L_{sim} + \gamma L_{cyc} + \lambda_1 L_{adv} + \lambda_2 L_{cls}, \quad (11)$$

$$L_D = -\lambda_3 \cdot L_{adv} + \lambda_4 \cdot L_{cls}, \quad (12)$$

where α , β , γ , λ_1 , λ_2 , λ_3 , and λ_4 are weightings for each loss item.

Table 1. Quantitative evaluation results for multisequence MRI synthesis on the BraTS dataset.

Input sequences				TransMI	TransMI _{uni}	MMGAN	ResViT	HF-GAN (ours)
T1	T2	T1c	FL	MAE / PSNR / SSIM / MS-SSIM				
✓	-	-	-	0.0136 / 29.30 / 0.9256 / 0.9352	0.0130 / 29.81 / 0.9316 / 0.9457	0.0154 / 29.30 / 0.9108 / 0.9395	0.0142 / 28.84 / 0.9137 / 0.9334	0.0126 / 30.00 / 0.9324 / 0.9472
-	✓	-	-	0.0141 / 29.61 / 0.9329 / 0.9460	0.0145 / 29.53 / 0.9337 / 0.9464	0.0173 / 28.81 / 0.9133 / 0.9384	0.0160 / 28.43 / 0.9135 / 0.9322	0.0137 / 29.92 / 0.9372 / 0.9499
-	-	✓	-	0.0151 / 28.73 / 0.9228 / 0.9371	0.0147 / 29.09 / 0.9280 / 0.9470	0.0166 / 28.47 / 0.9245 / 0.9403	0.0160 / 28.10 / 0.9116 / 0.9355	0.0143 / 29.28 / 0.9295 / 0.9479
-	-	-	✓	0.0148 / 28.67 / 0.9188 / 0.9300	0.0138 / 29.40 / 0.9288 / 0.9445	0.0164 / 28.70 / 0.9068 / 0.9379	0.0152 / 28.31 / 0.9114 / 0.9318	0.0134 / 29.53 / 0.9297 / 0.9458
Average				0.0144 / 29.08 / 0.9250 / 0.9371	0.0140 / 29.45 / 0.9305 / 0.9459	0.0164 / 28.82 / 0.9139 / 0.9390	0.0154 / 28.42 / 0.9125 / 0.9332	0.0135 / 29.68 / 0.9322 / 0.9477
✓	✓	-	-	- / - / - / -	0.0126 / 30.57 / 0.9358 / 0.9505	0.0154 / 29.88 / 0.9104 / 0.9422	0.0135 / 29.72 / 0.9203 / 0.9394	0.0117 / 31.07 / 0.9387 / 0.9543
✓	-	✓	-	- / - / - / -	0.0135 / 29.39 / 0.9302 / 0.9478	0.0154 / 28.83 / 0.9261 / 0.9410	0.0145 / 28.61 / 0.9158 / 0.9386	0.0129 / 29.80 / 0.9329 / 0.9509
✓	-	-	✓	- / - / - / -	0.0110 / 30.82 / 0.9454 / 0.9594	0.0133 / 30.30 / 0.9177 / 0.9548	0.0119 / 30.00 / 0.9346 / 0.9518	0.0104 / 31.22 / 0.9471 / 0.9619
-	✓	✓	-	- / - / - / -	0.0149 / 29.60 / 0.9388 / 0.9542	0.0173 / 28.78 / 0.9341 / 0.9453	0.0160 / 28.80 / 0.9248 / 0.9449	0.0140 / 30.11 / 0.9429 / 0.9583
-	✓	-	✓	- / - / - / -	0.0136 / 30.27 / 0.9446 / 0.9550	0.0165 / 29.44 / 0.9177 / 0.9481	0.0145 / 29.46 / 0.9315 / 0.9456	0.0126 / 30.75 / 0.9480 / 0.9587
-	-	✓	✓	- / - / - / -	0.0133 / 29.93 / 0.9446 / 0.9623	0.0154 / 29.14 / 0.9383 / 0.9558	0.0144 / 29.16 / 0.9333 / 0.9546	0.0126 / 30.38 / 0.9477 / 0.9650
Average				- / - / - / -	0.0132 / 30.10 / 0.9399 / 0.9549	0.0156 / 29.39 / 0.9240 / 0.9479	0.0141 / 29.29 / 0.9267 / 0.9458	0.0124 / 30.55 / 0.9429 / 0.9582
✓	✓	✓	-	- / - / - / -	0.0142 / 29.71 / 0.9302 / 0.9477	0.0168 / 28.76 / 0.9243 / 0.9359	0.0150 / 28.98 / 0.9149 / 0.9391	0.0133 / 30.27 / 0.9349 / 0.9524
✓	✓	-	✓	- / - / - / -	0.0106 / 31.93 / 0.9491 / 0.9578	0.0136 / 31.16 / 0.9017 / 0.9515	0.0110 / 31.28 / 0.9387 / 0.9504	0.0097 / 32.55 / 0.9521 / 0.9615
✓	-	✓	✓	- / - / - / -	0.0110 / 30.48 / 0.9501 / 0.9672	0.0125 / 29.81 / 0.9415 / 0.9623	0.0119 / 29.63 / 0.9411 / 0.9617	0.0103 / 31.06 / 0.9533 / 0.9703
-	✓	✓	✓	- / - / - / -	0.0150 / 30.13 / 0.9561 / 0.9661	0.0178 / 28.96 / 0.9493 / 0.9568	0.0159 / 29.36 / 0.9440 / 0.9573	0.0139 / 30.69 / 0.9595 / 0.9694
Average				- / - / - / -	0.0127 / 30.56 / 0.9463 / 0.9597	0.0152 / 29.67 / 0.9292 / 0.9516	0.0134 / 29.81 / 0.9347 / 0.9521	0.0118 / 31.14 / 0.9500 / 0.9634
Average (all)				- / - / - / -	0.0136 / 29.85 / 0.9366 / 0.9515	0.0160 / 29.13 / 0.9206 / 0.9444	0.0147 / 28.95 / 0.9215 / 0.9411	0.0129 / 30.22 / 0.9391 / 0.9542

3.5. Training scheme

For stable and robust training of our framework, we carefully select available sequences AS for L_{rec} and available sequences with synthesized image \hat{AS} for L_{sim} and L_{cyc} . Half of the mini-batch is used exclusively for the most difficult scenarios to compensate for the absent complementary information ($\Sigma AS = 1$ and $\Sigma \hat{AS} = 1$). The other half of the mini-batch randomly selects the initial available MR sequences except for extreme conditions ($\Sigma AS > 1$). To improve the extraction of complementary information and to construct valuable common spaces, we select the scenarios that produce the most informative feature representations ($\hat{AS} = N - 1$). Furthermore, for each subject, the network parameters are updated N times by employing all possible target sequences t , maximizing the use of MR compositions.

4. Experiments

4.1. Datasets

To validate the effectiveness of the proposed method, we have experimented with two public multisequence MRI datasets, the BraTS 2018 dataset (Bakas et al., 2017, 2018; Menze et al., 2014) and the IXI dataset¹.

BraTS 2018 is a patient brain MRI dataset comprising multiple institutional MRI scans of glioblastoma and lower-grade glioma. It consists of 285 subjects, each with four MR sequences: T1-weighted (T1), T2-weighted (T2), post-contrast T1-weighted (T1c), and T2-FLAIR (FL) MRIs. We partition the dataset into three subsets: 180 subjects for training, 20 subjects for validation, and 85 subjects for testing. For further data imputation experiments, the training dataset is divided into 80 subjects for training our framework and 100 subjects for training the segmentation network. Intensity normalization is performed by linearly scaling of the original intensities to the range $[-1, 1]$. During training, 2D axial slices are used, excluding those with less than 2000 brain pixels. The size of the final

images is set to 240×240 . The number of slices used for the training, validation, and test sets is 22,801, 2,511, and 10,745, respectively.

IXI Dataset consists of healthy brain MRI scans from three different institutions, each with three MR sequences: T1, T2, and PD-weighted (PD). The dataset includes 576 subjects in total; we divide them into training, validation, and test sets of 270, 30, and 276 subjects, respectively. In the preprocessing step, we first apply an affine transformation to the T1 and PD images to align them with the T2 images, by utilizing the NMI similarity metric through the use of the greedy registration tool (Yushkevich et al., 2016). The original intensities of the images are linearly adjusted to a range of $[-1, 1]$ with 99.5 percentile as the upper bound. During training, 2D axial slices are used, with 80 center axial slices specifically selected. The size of the final images is set to 256×256 . The number of slices used for the training, validation, and test sets is 21,600, 2,400, and 22,080, respectively.

4.2. Competing methods

We compare our unified framework with several state-of-the-art MR image synthesis methods, including TransMI (Cho et al., 2024), MMGAN (Sharma and Hamarneh, 2019), and ResViT (Dalmaz et al., 2022). TransMI is designed for one-to-one translation with a unified approach to use a single generator for all of the modality pairs. However, it can only synthesize N cases out of $2^N - 2$ missing cases, so we extend this work TransMI_{uni} to many-to-one using the multichannel early fusion encoder, while maintaining the unified approach. MMGAN and ResViT are a unified approach of many-to-many synthesize methods, and the results are produced using public code repositories^{2,3}. We evaluate all missing scenarios with 14 cases and 28 synthesis results for the BraTS dataset and 6 cases and 9 synthesis results for the IXI dataset, using four evaluation metrics including mean absolute error (MAE), peak signal-to-noise

¹<https://brain-development.org/ixi-dataset>

²<https://github.com/trane293/mm-gan>

³<https://github.com/icon-lab/ResViT>

Table 2. Quantitative evaluation results for multisequence MRI synthesis on the IXI dataset.

Input sequences			TransMI	TransMI _{uni}	MMGAN	ResViT	HF-GAN (ours)
T1	T2	PD	MAE / PSNR / SSIM / MS-SSIM	MAE / PSNR / SSIM / MS-SSIM			
✓	-	-	0.0269 / 24.95 / 0.8457 / 0.9425	0.0261 / 25.34 / 0.8574 / 0.9477	0.0298 / 24.11 / 0.8325 / 0.9317	0.0263 / 25.16 / 0.8502 / 0.9464	0.0257 / 25.47 / 0.8575 / 0.9486
-	✓	-	0.0198 / 28.75 / 0.9028 / 0.9664	0.0183 / 29.18 / 0.9222 / 0.9725	0.0215 / 27.87 / 0.9063 / 0.9656	0.0188 / 28.89 / 0.9249 / 0.9727	0.0180 / 29.36 / 0.9230 / 0.9731
-	-	✓	0.0185 / 28.71 / 0.9179 / 0.9710	0.0186 / 28.70 / 0.9176 / 0.9707	0.0217 / 27.32 / 0.9005 / 0.9623	0.0190 / 28.39 / 0.9181 / 0.9706	0.0181 / 28.87 / 0.9177 / 0.9714
Average			0.0217 / 27.47 / 0.8888 / 0.9600	0.0210 / 27.74 / 0.8990 / 0.9636	0.0244 / 26.43 / 0.8798 / 0.9532	0.0213 / 27.48 / 0.8978 / 0.9632	0.0206 / 27.90 / 0.8994 / 0.9644
✓	✓	-	- / - / - / -	0.0132 / 32.64 / 0.9463 / 0.9843	0.0160 / 30.85 / 0.9396 / 0.9806	0.0140 / 31.98 / 0.9481 / 0.9842	0.0125 / 33.09 / 0.9487 / 0.9855
✓	-	✓	- / - / - / -	0.0143 / 31.58 / 0.9343 / 0.9811	0.0164 / 30.12 / 0.9274 / 0.9774	0.0151 / 30.91 / 0.9356 / 0.9810	0.0137 / 31.96 / 0.9358 / 0.9824
-	✓	✓	- / - / - / -	0.0202 / 27.38 / 0.9163 / 0.9697	0.0233 / 26.47 / 0.8956 / 0.9628	0.0215 / 26.84 / 0.9118 / 0.9671	0.0198 / 27.53 / 0.9179 / 0.9703
Average			- / - / - / -	0.0159 / 30.53 / 0.9323 / 0.9784	0.0186 / 29.14 / 0.9209 / 0.9736	0.0169 / 29.91 / 0.9318 / 0.9775	0.0154 / 30.86 / 0.9341 / 0.9794
Average (all)			- / - / - / -	0.0193 / 28.67 / 0.9101 / 0.9686	0.0224 / 27.34 / 0.8935 / 0.9600	0.0199 / 28.29 / 0.9091 / 0.9680	0.0188 / 28.89 / 0.9110 / 0.9694

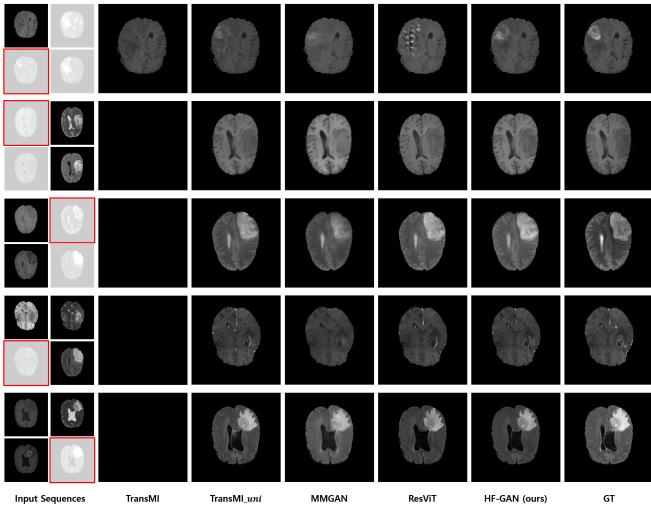


Fig. 4. An example of synthesized results for the missing MR sequence on the BraTS dataset. The first column represents the input MR sequences: T1, T2, FL, and T1c are located from the top-left in a clockwise direction. The target MR sequence (GT) is highlighted by a red border.

ratio (PSNR), structural similarity measure (SSIM), and multi-scale SSIM (MS-SSIM).

4.3. Implementation

Our framework is implemented using PyTorch, and all experiments in this study are carried out on a NVIDIA RTX 3090 GPU (24GB VRAM). The networks are optimized in 100 epochs using an Adam optimizer (Kingma and Ba, 2014) with $\beta_1 = 0.9$, $\beta_2 = 0.999$, and a batch size of 24 using gradient accumulation and half precision (fp16). We set initial learning rates of 0.0001 and 0.00001 for the generator and discriminator, respectively, with the cosine annealing scheduler (Loshchilov and Hutter, 2016), which has a short warm-up phase and then decays to zero afterward. The weighting of the loss components is configured as follows: $\alpha = 10$, $\beta = 1$, $\gamma = 1$, $\lambda_1 = 0.25$, $\lambda_2 = 0.25$, $\lambda_3 = 0.25$, and $\lambda_4 = 0.25$. Our source code is available on <https://github.com/SSTDV-Project/HF-GAN>.

4.4. Multisequence MRI synthesis

Table 1 and Figure 4 present the evaluation results on the BraTS dataset. Due to the varying appearance of brain tumors

in different sequences, it is essential to extract complementary features and project them into an appropriate latent space for accurate synthesis, in particular, when the available information is limited. When a single modality is provided, the one-to-one unified approach TransMI shows worse results than its extension TransMI_{uni}. The capability of TransMI_{uni} to handle all missing scenarios results in a performance improvement in 0.0004 for MAE, 0.37 for PSNR, 0.0055 for SSIM, and 0.088 for MS-SSIM, with effective latent space. As shown in the first row of Figure 4, ResViT faces challenges with the latent space. It struggles to synthesize tumor regions when the information provided is scarce with the worst results of 0.0154 for MAE, 28.42 for PSNR, 0.9125 for SSIM, and 0.9332 for MS-SSIM, while it achieves great synthesized results when sufficient information is available. Therefore, relying solely on the transformer architecture is not sufficient to construct a robust latent space, especially when dealing with limited data in medical imaging. MMGAN shows satisfactory performance across all missing scenarios with 0.0160 for MAE, 29.13 for PSNR, 0.9206 for SSIM, and 0.9444 for MS-SSIM. However, the synthesis of tumor regions is relatively less effective due to the limited complementary information. In contrast, our method outperforms all state-of-the-art methods across all missing scenarios, achieving an average of 0.0129 for MAE, 30.22 for PSNR, 0.9391 for SSIM, and 0.9542 for MS-SSIM. Performance improvement in all scenarios demonstrates the superiority of our proposed hybrid fusion encoder and channel attention-based feature fusion

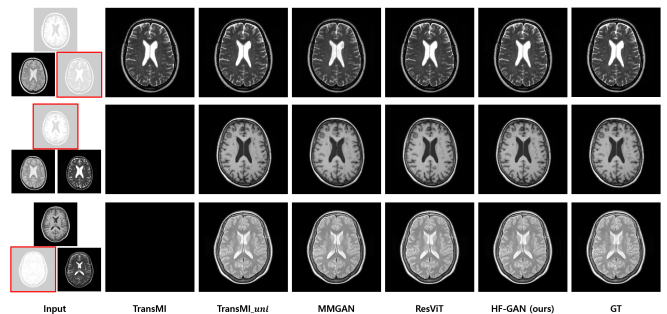


Fig. 5. An example of synthesized results for the missing MR sequence on the IXI dataset. The first column represents the input MR sequences: T1, T2, and PD are located from the top in a clockwise direction. The target MR sequence (GT) is highlighted by a red border.

Table 3. Brain tumor segmentation results with data imputation on the BraTS dataset. The results represent the average Dice score over 85 test subjects and WT, TC, and ET stand for whole tumor, tumor core, and enhanced tumor, respectively. Ours (w/o CI) is the image synthesis performed without the integration of complementary information. When only a single MR sequence is available, our framework does not utilize complementary information, resulting in identical synthesized results.

Available sequences				Data imputation method														
				Zero intensity			Synthesized from MMGAN			Synthesized from ResViT			Synthesized from HF-GAN (ours)			Synthesized from HF-GAN (w/o CI)		
T1	T2	T1c	FL	WT	TC	ET	WT	TC	ET	WT	TC	ET	WT	TC	ET	WT	TC	ET
✓	-	-	-	0.0000 / 0.0000 / 0.0824	0.5323 / 0.3917 / 0.1212	0.1402 / 0.0699 / 0.0847	0.7108 / 0.5119 / 0.0842	0.7365 / 0.5465 / 0.2326	0.5806 / 0.4335 / 0.1440	0.5806 / 0.4335 / 0.1440	0.5806 / 0.4335 / 0.1440							
-	✓	-	-	0.3865 / 0.1387 / 0.0985	0.7274 / 0.5549 / 0.1545	0.7108 / 0.5119 / 0.0842	0.7365 / 0.5465 / 0.2326	0.5806 / 0.4335 / 0.1440	0.5806 / 0.4335 / 0.1440	0.5806 / 0.4335 / 0.1440								
-	-	✓	-	0.0000 / 0.0000 / 0.0824	0.5511 / 0.4363 / 0.6116	0.4599 / 0.3454 / 0.5931	0.7365 / 0.5465 / 0.2326	0.5806 / 0.4335 / 0.1440	0.5806 / 0.4335 / 0.1440	0.5806 / 0.4335 / 0.1440								
-	-	-	✓	0.0837 / 0.0749 / 0.1084	0.7854 / 0.6431 / 0.1482	0.7365 / 0.5465 / 0.2326	0.7365 / 0.5465 / 0.2326	0.5806 / 0.4335 / 0.1440	0.5806 / 0.4335 / 0.1440	0.5806 / 0.4335 / 0.1440								
Average				0.1175 / 0.0534 / 0.0929	0.6490 / 0.5065 / 0.2589	0.5118 / 0.3684 / 0.2487	0.7365 / 0.5465 / 0.2326	0.5806 / 0.4335 / 0.1440	0.5806 / 0.4335 / 0.1440	0.5806 / 0.4335 / 0.1440								
✓	✓	-	-	0.0829 / 0.0167 / 0.0824	0.7476 / 0.5890 / 0.1476	0.7355 / 0.5771 / 0.1084	0.7355 / 0.5771 / 0.1084	0.8057 / 0.6543 / 0.1895	0.8057 / 0.6543 / 0.1895	0.8057 / 0.6543 / 0.1895								
✓	-	✓	-	0.0003 / 0.0002 / 0.0830	0.5983 / 0.4786 / 0.6653	0.2651 / 0.2091 / 0.4976	0.2651 / 0.2091 / 0.4976	0.8550 / 0.7190 / 0.2044	0.8550 / 0.7190 / 0.2044	0.8550 / 0.7190 / 0.2044								
✓	-	-	✓	0.5383 / 0.4540 / 0.1807	0.8352 / 0.6921 / 0.1497	0.8201 / 0.6423 / 0.1665	0.8201 / 0.6423 / 0.1665	0.8200 / 0.6983 / 0.7650	0.8200 / 0.6983 / 0.7650	0.8200 / 0.6983 / 0.7650								
-	✓	✓	-	0.3325 / 0.2110 / 0.4098	0.7659 / 0.6411 / 0.7369	0.8556 / 0.7023 / 0.2293	0.8556 / 0.7023 / 0.2293	0.8672 / 0.7172 / 0.2589	0.8672 / 0.7172 / 0.2589	0.8672 / 0.7172 / 0.2589								
-	-	✓	✓	0.8428 / 0.6758 / 0.2294	0.8487 / 0.6905 / 0.1551	0.8293 / 0.6947 / 0.7464	0.8293 / 0.6947 / 0.7464	0.8715 / 0.7668 / 0.7742	0.8715 / 0.7668 / 0.7742	0.8715 / 0.7668 / 0.7742								
-	-	-	✓	0.2007 / 0.1912 / 0.1566	0.8488 / 0.7283 / 0.7530	0.8293 / 0.6947 / 0.7464	0.8293 / 0.6947 / 0.7464	0.8715 / 0.7668 / 0.7742	0.8715 / 0.7668 / 0.7742	0.8715 / 0.7668 / 0.7742								
Average				0.3329 / 0.2581 / 0.1903	0.7741 / 0.6366 / 0.4346	0.7209 / 0.5873 / 0.4189	0.7209 / 0.5873 / 0.4189	0.8126 / 0.6814 / 0.4844	0.8126 / 0.6814 / 0.4844	0.8126 / 0.6814 / 0.4844								
✓	✓	✓	-	0.2679 / 0.1733 / 0.4505	0.7754 / 0.6588 / 0.7437	0.7653 / 0.6513 / 0.7533	0.7653 / 0.6513 / 0.7533	0.8228 / 0.7105 / 0.7842	0.8228 / 0.7105 / 0.7842	0.8228 / 0.7105 / 0.7842								
✓	✓	-	✓	0.8503 / 0.6962 / 0.2376	0.8614 / 0.7189 / 0.1529	0.8632 / 0.7011 / 0.2128	0.8632 / 0.7011 / 0.2128	0.8714 / 0.7289 / 0.2207	0.8714 / 0.7289 / 0.2207	0.8714 / 0.7289 / 0.2207								
✓	-	✓	✓	0.4983 / 0.4325 / 0.5341	0.8610 / 0.7584 / 0.7751	0.8566 / 0.7502 / 0.7805	0.8566 / 0.7502 / 0.7805	0.8697 / 0.7700 / 0.7785	0.8697 / 0.7700 / 0.7785	0.8697 / 0.7700 / 0.7785								
-	✓	✓	✓	0.8620 / 0.7500 / 0.7607	0.8766 / 0.7626 / 0.7839	0.8769 / 0.7686 / 0.7785	0.8769 / 0.7686 / 0.7785	0.8832 / 0.7794 / 0.7918	0.8832 / 0.7794 / 0.7918	0.8832 / 0.7794 / 0.7918								
Average				0.6196 / 0.5130 / 0.4957	0.8436 / 0.7247 / 0.6139	0.8405 / 0.7178 / 0.6313	0.8405 / 0.7178 / 0.6313	0.8618 / 0.7472 / 0.6438	0.8618 / 0.7472 / 0.6438	0.8618 / 0.7472 / 0.6438								
Average				0.3533 / 0.2725 / 0.2498	0.7582 / 0.6246 / 0.4356	0.6954 / 0.5620 / 0.4309	0.6954 / 0.5620 / 0.4309	0.7963 / 0.6665 / 0.4824	0.7963 / 0.6665 / 0.4824	0.7963 / 0.6665 / 0.4824								

method. In addition, precise synthesized results with better details in tumor regions ensure the effective extraction of complementary information and demonstrate the capability of feature-level latent space conversion by the modality infuser.

For the IXI dataset, which contains healthy brain images, the importance of complementary information is relatively limited to the contrast details of each sequence. Therefore, as shown in Figure 5, most of the methods show outstanding synthesized results compared to the BraTS dataset. In the quantitative evaluation, as detailed in Table 2, TransMI_{uni} shows better performance than TransMI with 0.007 for MAE, 0.27 for PSNR, 0.0102 for SSIM, and 0.0036 for MS-SSIM when a single MR sequence is available. ResViT demonstrates the superiority of the Transformer in achieving better results for all metrics compared to MMGAN due to the reduced complexity of missing scenarios (6 cases). However, our approach of constructing a robust latent space that emphasizes complementary information still achieves the highest performance in all scenarios, with averages of 0.0188 for MAE, 28.89 for PSNR, 0.9110 for SSIM, and 0.9694 for MS-SSIM, except for the SSIM metric in two out of six cases. The accurate synthesized results of HF-GAN, regardless of input compositions, highlight the superiority of our proposed framework and demonstrate the importance of complementary information in multisequence MRI synthesis.

4.5. Data imputation for segmentation

To achieve promising results with the automatic segmentation method, it is essential to prepare input compositions that match those used in the training. Typically, automatic brain tumor segmentation utilizes all four MR sequences: T1, T2, T1c, and FL, as they provide complementary information. In practical situations, certain MR sequences may be missing, and the synthesis of images from the available sequences can help to take advantage of automatic segmentation methods.

To validate the effectiveness of data imputation through our synthesis framework, we train a state-of-the-art segmentation

network (Isensee et al., 2021), which has shown top performance on numerous medical image segmentation datasets, including the BraTS dataset (Luu and Park, 2021). It achieves Dice scores of 0.8819, 0.7818, and 0.7908 for the whole tumor (WT), tumor core (TC), and enhanced tumor (ET) regions, respectively, using all four MR sequences. The segmentation results with data imputation are summarized in Table 3. The results show that the data imputation method using our synthesis framework outperforms the other methods. The use of zero-intensity imputation gives poor results, with average Dice scores of 0.3533, 0.2725, and 0.2498, even in the presence of brain tumor information. When data imputation is performed by image synthesis through MMGAN, the results are better than with ResViT with an improvement of 0.0628 for WT, 0.0518 for TC, and 0.0047 for ET due to poor synthesis results when available sequences are limited, as discussed in subsection 4.4. Compared to these methods, our approach shows robust segmentation results with average Dice scores of 0.7064, 0.5633, and 0.3178. Our approach using only T1c and FL also shows performance comparable to that of using all MR sequences, with only slight reductions of 0.0104, 0.0150, and 0.0166 for WT, TC, and ET, respectively. In addition, the absence of complementary information, in particular, leads to a decrease in segmentation performance. This suggests that the complementary features provided by our framework affect the finer details of brain tumor regions more than the overall structural information. An investigation of complementary information is provided in subsection 4.6.

4.6. Analysis of latent space and complementary information

Our unified framework is based on the disentanglement of feature extraction and latent space. The hybrid fusion encoder independently extracts features that include complementary features from the early fusion encoder and modality-specific features from the middle fusion encoders. These features are projected into the latent space using *CAFF*, where the latent

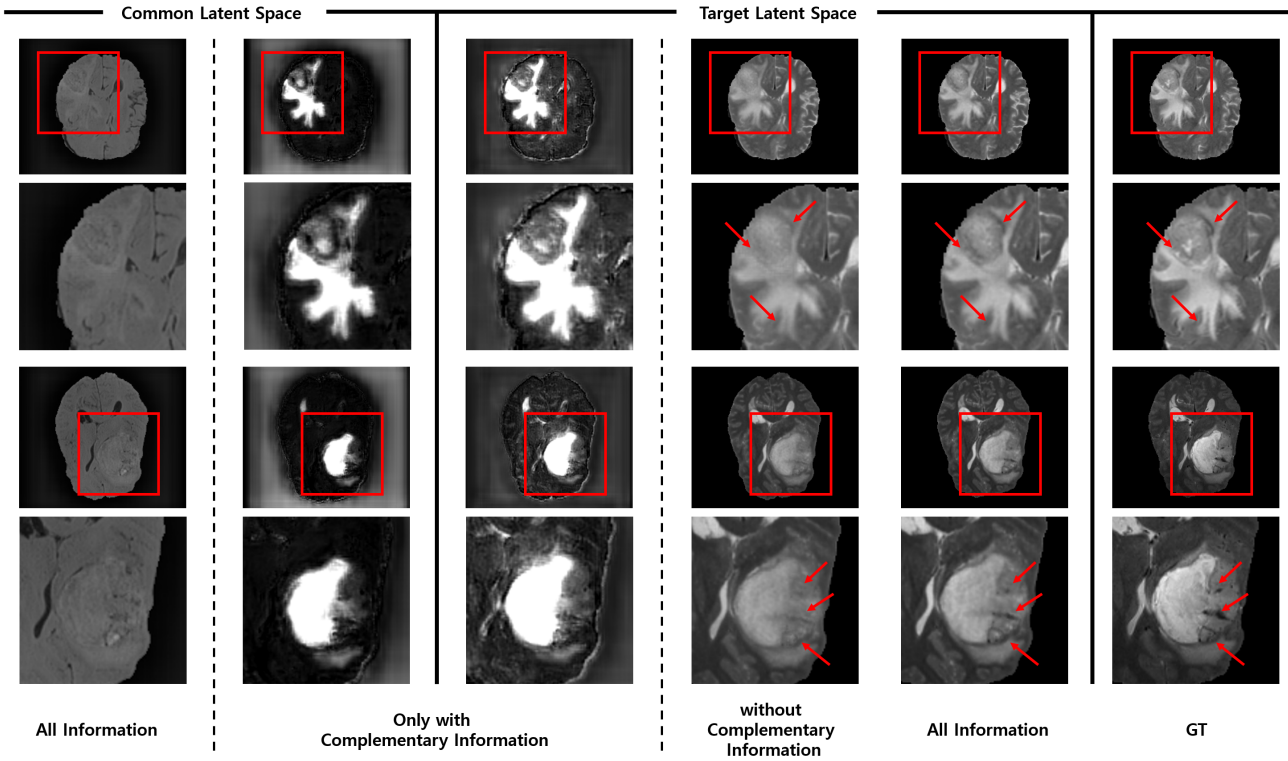


Fig. 6. Image synthesis results of different feature representations when the same MR images are used. The feature representations in the common latent space are used to synthesize the images in the first and second columns, while the feature representations in the target (T2) latent space are used to synthesize the images in the third to fifth columns. Each column is synthesized from three distinct feature representations: 1) using all extracted features (all information), 2) using only features from the early fusion encoder (only with complementary information), and 3) using only features from the middle fusion encoders (without complementary information).

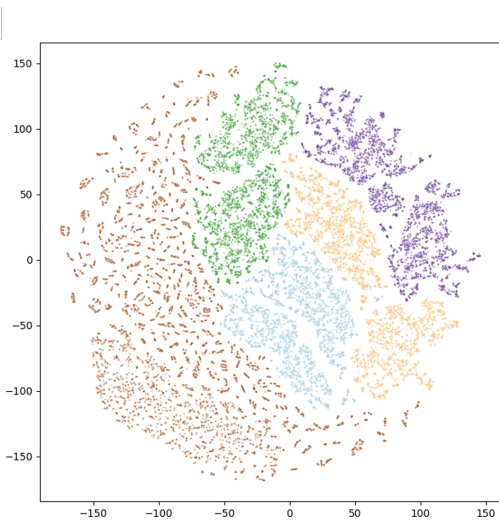


Fig. 7. T-SNE visualization of common latent space and target latent space. A total of 21,000 feature representations are depicted, covering all 14 missing scenarios. The brown color illustrates the common feature representations, while the other colors indicate the feature representations within the target latent spaces transformed by the modality infuser. T1 is shown in blue, T2 in green, T1c in yellow, and FL in purple.

space is divided into a common latent space to handle all missing scenarios and a target latent space to synthesize missing MR sequences. Figure 6 shows the actual effect of their separation in the synthesis process. The images synthesized from the common latent space have low contrast but retain structural details, while the synthesis that uses only early fusion features highlights the regions of brain tumors containing the most complementary information. These features are then converted using the modality infuser, and each latent space is properly disentangled, as shown in Figure 7, allowing the synthesis of the appropriate contrast. As shown in the third to fifth columns of Figure 6, the characteristics of the target sequences are reflected in the synthesized images even when only early fusion features are used. In addition, we conduct experiments to confirm the advantage of complementary features, as seen in columns four and five. When complementary features are omitted from the synthesis process, the synthesized images appear less distinct, especially in the tumor regions, than when all features are included. This shows that our hybrid fusion encoder is capable of effectively separating and extracting complementary information, resulting in accurate synthesis results, especially in tumor regions.

4.7. Ablation Study

To verify the effectiveness of our proposed framework, we perform an ablation study using the BraTS dataset. We first

Table 4. Evaluation results of our method and its variants, with the hybrid fusion encoder and channel attention-based feature fusion ablated. The results are averaged over all missing scenarios.

Methods	Results			
	MAE	PSNR	SSIM	MS-SSIM
Ours (w/o Enc^{MF})	0.0151	29.19	0.9333	0.9446
Ours (w/o Enc^{EF})	0.0144	29.41	0.9324	0.9459
Ours (w/o $CAFF$)	0.0145	29.40	0.9331	0.9456
Ours	0.0139	29.67	0.9354	0.9486

evaluate the key components for the construction of common latent space, followed by an investigation of the modality encoding approach of the modality infuser for target conditioning.

The basic concept of the hybrid fusion approach is the separate extraction of complementary and modality-specific information. To achieve this, both the early fusion encoder Enc^{EF} and the middle fusion encoders Enc^{MF} are used, where Enc^{EF} is responsible for extracting complementary information between the MR sequences, and Enc^{MF} emphasizes the structural information for each MR sequence. Table 4 presents the evaluation results with different compositions. Without Enc^{MF} , our framework faces difficulties as it needs to simultaneously extract both shared and complementary information, leading to notable performance drops of 0.012 for MAE, 0.48 for PSNR, 0.0021 for SSIM, and 0.004 for MS-SSIM. In the absence of Enc^{EF} , the MR sequences do not interact during the feature extraction phase, resulting in a lack of complementary information and subsequent performance degradation. However, the simple use of both encoders without the channel attention-based feature fusion module $CAFF$ is also not sufficient to establish a robust common latent space, resulting in significant performance degradation. This shows that complementary information and modality-specific information are fundamentally distinct.

The feature representations in the common latent space are converted into the target latent space via the modality infuser. The modality encoding module within the modality infuser is responsible for this feature-level transformation. The modality encoding is similar to the positional encoding used in Transformers. However, the primary difference is that the modality encoding modifies all 1D tokens uniformly to transform the entire feature set into the target latent space, whereas positional encoding adds values to differentiate individual tokens. Therefore, as shown in Table 5, learnable parameters initialized to zero do not train effectively due to an insufficient conversion

Table 5. Evaluation results of the modality encoding methods of the modality infuser. The results are averaged over all missing scenarios.

Modality Encoding	Results			
	MAE	PSNR	SSIM	MS-SSIM
learnable parameter	0.0194	26.79	0.8986	0.8861
sinusoidal function	0.0153	28.81	0.9258	0.9381
one-hot vector + MLP	0.0140	29.63	0.9353	0.9482
sinusoidal function + MLP	0.0139	29.67	0.9354	0.9486

force. The sinusoidal function provides distinct values for the target modality, but it is also less effective since it lacks trainable parameters. A possible solution is to use learnable parameters for distinct target indicators. We experiment with two types of indicators: one-hot vectors and sinusoidal functions. There are no significant differences between them, but the sinusoidal function shows better results by converging faster than the one-hot vector.

5. Conclusion and Future Work

In this work, we propose a unified synthesis framework for multisequence MRI. We design a hybrid fusion encoder that facilitates the extraction of complementary information, coupled with a feature fusion module that uses channel attention to construct a robust common latent space and a modality infuser that enables an efficient synthesis of the target sequence. Experimental results demonstrate that our method can achieve state-of-the-art performance in multisequence MRI synthesis and show potential for data imputation applications. We further investigate the impact of our designed components and perform an ablation study to confirm their effectiveness.

While our method shows superior results both quantitatively and qualitatively, we note that there are still certain limitations. The use of multiple encoders to construct a common latent space can result in high memory consumption, especially when dealing with a large number of modalities. As in our previous work (Cho et al., 2024), the use of a weight-shared encoder could be a potential solution, although it involves a trade-off between performance and memory efficiency. Our framework is specifically designed for spatially registered datasets, but it requires additional time for atlas-based image registration. Nevertheless, our framework has the potential to be applied to unpaired datasets, since our training loss includes both the reconstruction loss for spatially aligned images and the cycle-consistency loss applicable to unpaired datasets. Therefore, extending our approach to unpaired datasets, including translation between MRI and CT, is part of our future work.

In addition, we are interested in developing a robust segmentation network that does not require all MR sequences, taking advantage of a common latent space (Chen et al., 2019; Ding et al., 2021; Dorent et al., 2019). Since an accurate image synthesis of brain tumor regions is facilitated by constructing a common latent space that highlights complementary information, this approach is also expected to improve image segmentation performance.

Acknowledgments

This work was supported by Institute for Information & communications Technology Promotion(IITP) grant funded by the Korea government (MSIT) (No.00223446, Development of object-oriented synthetic data generation and evaluation methods) and the Technology Innovation Program (20011875, Development of AI-Based Diagnostic Technology for Medical Imaging Devices) funded by the Ministry of Trade, Industry & Energy (MOTIE, Korea).

References

- Bakas, S., Akbari, H., Sotiras, A., Bilello, M., Rozycki, M., Kirby, J.S., Freymann, J.B., Farahani, K., Davatzikos, C., 2017. Advancing the cancer genome atlas glioma mri collections with expert segmentation labels and radiomic features. *Scientific data* 4, 1–13.
- Bakas, S., Reyes, M., Jakab, A., Bauer, S., Rempfler, M., Crimi, A., Shinozaki, R.T., Berger, C., Ha, S.M., Rozycki, M., et al., 2018. Identifying the best machine learning algorithms for brain tumor segmentation, progression assessment, and overall survival prediction in the brats challenge. *arXiv preprint arXiv:1811.02629*.
- Chan, H.P., Hadjiiski, L.M., Samala, R.K., 2020. Computer-aided diagnosis in the era of deep learning. *Medical physics* 47, e218–e227.
- Chartsias, A., Joyce, T., Giuffrida, M.V., Tsaftaris, S.A., 2017. Multimodal mr synthesis via modality-invariant latent representation. *IEEE transactions on medical imaging* 37, 803–814.
- Chen, C., Dou, Q., Jin, Y., Chen, H., Qin, J., Heng, P.A., 2019. Robust multimodal brain tumor segmentation via feature disentanglement and gated fusion, in: *Medical Image Computing and Computer Assisted Intervention–MICCAI 2019: 22nd International Conference, Shenzhen, China, October 13–17, 2019, Proceedings, Part III 22, Springer*. pp. 447–456.
- Cho, J., Liu, X., Xing, F., Ouyang, J., El Fakhri, G., Park, J., Woo, J., 2024. Disentangled multimodal brain mr image translation via transformer-based modality infuser, in: *Medical Imaging 2024: Image Processing, SPIE*. pp. 602–607.
- Cho, J., Park, J., 2023. Hybrid-fusion transformer for multisequence mri, in: *Su, R., Zhang, Y., Liu, H., Frangi, A. (Eds.), Medical Imaging and Computer-Aided Diagnosis, Springer Nature Singapore, Singapore*. pp. 477–487.
- Dalmaz, O., Yurt, M., Çukur, T., 2022. Resvit: residual vision transformers for multimodal medical image synthesis. *IEEE Transactions on Medical Imaging* 41, 2598–2614.
- Dar, S., Yurt, M., Karacan, L., Erdem, A., Erdem, E., Çukur, T., 2019. Image synthesis in multi-contrast MRI with conditional generative adversarial networks. *IEEE TMI*, 2375–2388.
- Ding, Y., Yu, X., Yang, Y., 2021. Rfnet: Region-aware fusion network for incomplete multi-modal brain tumor segmentation, in: *Proceedings of the IEEE/CVF international conference on computer vision*. pp. 3975–3984.
- Dorent, R., Joutard, S., Modat, M., Ourselin, S., Vercauteren, T., 2019. Hetero-modal variational encoder-decoder for joint modality completion and segmentation, in: *Medical Image Computing and Computer Assisted Intervention–MICCAI 2019: 22nd International Conference, Shenzhen, China, October 13–17, 2019, Proceedings, Part II 22, Springer*. pp. 74–82.
- Dosovitskiy, A., Beyer, L., Kolesnikov, A., Weissenborn, D., Zhai, X., Unterthiner, T., Dehghani, M., Minderer, M., Heigold, G., Gelly, S., et al., 2020. An image is worth 16x16 words: Transformers for image recognition at scale. *arXiv preprint arXiv:2010.11929*.
- Elfwing, S., Uchibe, E., Doya, K., 2018. Sigmoid-weighted linear units for neural network function approximation in reinforcement learning. *Neural networks* 107, 3–11.
- Goodfellow, I., Pouget-Abadie, J., Mirza, M., Xu, B., Warde-Farley, D., Ozair, S., Courville, A., Bengio, Y., 2014. Generative adversarial nets, in: *Advances in neural information processing systems*. pp. 2672–2680.
- Isensee, F., Jaeger, P.F., Kohl, S.A., Petersen, J., Maier-Hein, K.H., 2021. nnu-net: a self-configuring method for deep learning-based biomedical image segmentation. *Nature methods* 18, 203–211.
- Isola, P., Zhu, J.Y., Zhou, T., Efros, A.A., 2017. Image-to-image translation with conditional adversarial networks, in: *Proceedings of the IEEE conference on computer vision and pattern recognition*. pp. 1125–1134.
- Jog, A., Carass, A., Roy, S., Pham, D.L., Prince, J.L., 2017. Random forest regression for magnetic resonance image synthesis. *Medical image analysis* 35, 475–488.
- Kingma, D.P., Ba, J., 2014. Adam: A method for stochastic optimization. *arXiv preprint arXiv:1412.6980*.
- Lee, D., Moon, W.J., Ye, J.C., 2020. Assessing the importance of magnetic resonance contrasts using collaborative generative adversarial networks. *Nature Machine Intelligence* 2, 34–42.
- Lee, J., Carass, A., Jog, A., Zhao, C., Prince, J.L., 2017. Multi-atlas-based ct synthesis from conventional mri with patch-based refinement for mri-based radiotherapy planning, in: *Medical Imaging 2017: Image Processing, SPIE*. pp. 434–439.
- Li, H., Paetzold, J.C., Sekuboyina, A., Kofler, F., Zhang, J., Kirschke, J.S., Wiestler, B., Menze, B., 2019. Diamondgan: unified multi-modal generative adversarial networks for mri sequences synthesis, in: *Medical Image Computing and Computer Assisted Intervention–MICCAI 2019: 22nd International Conference, Shenzhen, China, October 13–17, 2019, Proceedings, Part IV 22, Springer*. pp. 795–803.
- Liu, J., Pasumarthi, S., Duffy, B., Gong, E., Datta, K., Zaharchuk, G., 2023. One model to synthesize them all: Multi-contrast multi-scale transformer for missing data imputation. *IEEE Transactions on Medical Imaging*.
- Liu, X., Xing, F., El Fakhri, G., Woo, J., 2021. A unified conditional disentanglement framework for multimodal brain mr image translation, in: *2021 IEEE 18th International Symposium on Biomedical Imaging (ISBI), IEEE*. pp. 10–14.
- Loshchilov, I., Hutter, F., 2016. Sgdr: Stochastic gradient descent with warm restarts. *arXiv preprint arXiv:1608.03983*.
- Luu, H.M., Park, S.H., 2021. Extending nn-unet for brain tumor segmentation, in: *International MICCAI brainlesion workshop, Springer*. pp. 173–186.
- Menze, B.H., Jakab, A., Bauer, S., Kalpathy-Cramer, J., Farahani, K., et al., 2014. The multimodal brain tumor image segmentation benchmark (brats). *IEEE TMI*.
- Mirza, M., Osindero, S., 2014. Conditional generative adversarial nets. *arXiv preprint arXiv:1411.1784*.
- Odena, A., Olah, C., Shlens, J., 2017. Conditional image synthesis with auxiliary classifier gans, in: *ICML*.
- Schouten, T.M., Koini, M., De Vos, F., Seiler, S., Van Der Grond, J., Lechner, A., Hafkemeijer, A., Möller, C., Schmidt, R., De Rooij, M., et al., 2016. Combining anatomical, diffusion, and resting state functional magnetic resonance imaging for individual classification of mild and moderate alzheimer’s disease. *NeuroImage: Clinical* 11, 46–51.
- Sevetlidis, V., Giuffrida, M.V., Tsaftaris, S.A., 2016. Whole image synthesis using a deep encoder-decoder network, in: *Simulation and Synthesis in Medical Imaging: First International Workshop, SASHIMI 2016, Held in Conjunction with MICCAI 2016, Athens, Greece, October 21, 2016, Proceedings 1, Springer*. pp. 127–137.
- Sharma, A., Hamarneh, G., 2019. Missing mri pulse sequence synthesis using multi-modal generative adversarial network. *IEEE transactions on medical imaging* 39, 1170–1183.
- Wu, Y., He, K., 2018. Group normalization, in: *Proceedings of the European conference on computer vision (ECCV)*. pp. 3–19.
- Xin, B., Hu, Y., Zheng, Y., Liao, H., 2020. Multi-modality generative adversarial networks with tumor consistency loss for brain mr image synthesis, in: *2020 IEEE 17th international symposium on biomedical imaging (ISBI), IEEE*. pp. 1803–1807.
- Yang, H., Sun, J., Yang, L., Xu, Z., 2021. A unified hyper-gan model for unpaired multi-contrast mr image translation, in: *Medical Image Computing and Computer Assisted Intervention–MICCAI 2021: 24th International Conference, Strasbourg, France, September 27–October 1, 2021, Proceedings, Part III 24, Springer*. pp. 127–137.
- Ye, D.H., Zikic, D., Glocker, B., Criminisi, A., Konukoglu, E., 2013. Modality propagation: coherent synthesis of subject-specific scans with data-driven regularization, in: *Medical Image Computing and Computer-Assisted Intervention–MICCAI 2013: 16th International Conference, Nagoya, Japan, September 22–26, 2013, Proceedings, Part I 16, Springer*. pp. 606–613.
- Yurt, M., Dar, S.U., Erdem, A., Erdem, E., Ogun, K.K., Çukur, T., 2021. must-gan: multi-stream generative adversarial networks for mr image synthesis. *Medical image analysis* 70, 101944.
- Yushkevich, P.A., Pluta, J., Wang, H., Wisse, L.E., Das, S., Wolk, D., 2016. Ic-p-174: fast automatic segmentation of hippocampal subfields and medial temporal lobe subregions in 3 tesla and 7 tesla t2-weighted mri. *Alzheimer’s & Dementia* 12, P126–P127.
- Zhou, T., Fu, H., Chen, G., Shen, J., Shao, L., 2020. Hi-net: hybrid-fusion network for multi-modal mr image synthesis. *IEEE transactions on medical imaging* 39, 2772–2781.
- Zhu, J.Y., Park, T., Isola, P., Efros, A.A., 2017. Unpaired image-to-image translation using cycle-consistent adversarial networks, in: *Proceedings of the IEEE international conference on computer vision*. pp. 2223–2232.